Research Article Vol. 17, No. 2 / 1 Feb 2026 / Biomedical Optics Express 1064
Biomedical Optics EXPRESS

Thermal lensing effects in two-photon light-sheet microscopy

ANTOINE HUBERT,[1,2] HUGO TRENTESAUX,[1,2] THOMAS PUJOL,[1,2] GEORGES DEBRÉGEAS,[1,2] AND VOLKER BORMUTH[1,2,*]

[1]Sorbonne Université, CNRS, Laboratoire Jean Perrin, LJP, F-75005 Paris, France
[2]Sorbonne Université, CNRS, Inserm, Institut de Biologie Paris-Seine, IBPS, F75005 Paris, France
[*]volker.bormuth@sorbonne-universite.fr

Abstract: In light-sheet fluorescence microscopy (LSFM), the axial resolution is governed by the illumination beam profile, motivating the development of advanced beam-shaping techniques to enhance imaging performance. Two-photon LSFM (2P-LSFM), in particular, improves the signal-to-background ratio by reducing laser scattering and distortion in biological specimens. However, we report a potentially detrimental thermal effect in 2P-LSFM: the high laser powers required for two-photon excitation induce localized heating, which alters the refractive index of the medium and effectively forms a divergent thermal lens in water. At 500 mW, the light-sheet waist broadens by 25% and shifts by 300 μm before stabilizing several seconds after the laser shutter is opened. Both experiments and simulations reveal that this thermal lensing effect scales with laser power and the path length the beam travels through water. The resulting degradation in resolution and signal-to-noise ratio may compromise imaging applications that require high laser powers for rapid volumetric imaging of large specimens or functional brain imaging. This limitation is particularly critical in dynamic sample environments, such as during stepwise repositioning or flow-based delivery of chemical or hydrodynamic sensory stimuli, where changes occur on timescales comparable to the thermal settling time.

1. Introduction

Since its introduction more than two decades ago [1], light-sheet fluorescence microscopy (LSFM) has become a key imaging technique in developmental biology and neuroscience, enabling high-resolution imaging of *in vivo* and cleared samples [2–4]. Its ability to perform rapid volumetric acquisition makes it well-suited for functional imaging combined with behavioral studies, or large field-of-view imaging at single-cell resolution in 3D [2,5–7].

Multiphoton light-sheet microscopy (2P-LSFM or 3P-LSFM) has later emerged as a powerful alternative for denser tissue by offering reduced scattering and greater penetration depth due to infrared excitation [8–11]. Importantly, it is also particularly well suited for imaging living organisms, as most biological tissues exhibit minimal sensitivity to infrared light. This characteristic significantly reduces visual biases associated with 1P-LSFM, which can interfere with behavior or neuronal activity, particularly in systems such as zebrafish larva [12,13]. However, like all multiphoton techniques, it imposes constraints related to photodamage and heat deposition [14]. Beyond these biological limitations, beam propagation through aqueous media, particularly in long working distance configurations, can introduce additional thermal effects that pose questions about their influence on imaging performance.

Thermal effects are documented in various applications involving high-power lasers, typically in the range of tens to hundreds of watts. For instance, acousto-optic modulators (AOMs) crystals made of TeO_2 are known to induce a converging lens effect within the material, resulting in focal mismatches [15]. In applications such as optical trapping and laser cutting or optical cavities, these thermal effects must be carefully considered to ensure precise beam control and system

#564339 https://doi.org/10.1364/BOE.564339
Journal © 2026 Received 11 Apr 2025; revised 25 Jun 2025; accepted 28 Jun 2025; published 29 Jan 2026

Biomedical Optics EXPRESS

performance [15,16]. The effects of laser-induced thermal lenses on liquids can also be used as a means to measure the thermo-optical coefficient of a solution [17].

In this study, we aim to provide a detailed experimental characterization of the thermal lens effect in the specific context of 2P-LSFM. We examined the relationship between waist size and focal position in relation to laser power and the propagation distance of the laser through water. Additionally, we characterized the settling dynamics and stability of the thermally induced focal shift from the time the laser was switched on. We then developed and implemented simulations to investigate these dynamics further. Integrating experimental observations with simulations allowed us to identify key factors affecting the stability and shape of high-power laser beams focused through liquids, highlighting critical considerations for optimizing performance in 2P-LSFM applications.

2. Material and methods

To investigate the impact of thermal lensing on beam propagation in 2P-LSFM, we directly visualized the laser forming the digitally scanned light sheet using the microscope's detection objective (see Fig. 1(A)). The laser beam was propagated through a water-filled tank containing a low concentration of saturated Rhodamine 6G, which enabled two-photon excitation of the dye. This configuration allowed us to image the fluorescence—and hence the laser beam—perpendicular to its propagation axis.

Our infrared source was a pulsed infrared laser (Coherent, Monaco, 40 W, 1035 nm, 273 fs pulses, 50 MHz repetition rate). The light sheet was formed using a 5X IR objective (Olympus LMPLN5XIR, NA = 0.1, WD = 16 mm) that focused the laser first through air and then through a thin cover glass (130-160 μm thickness, Menzel Gläser #1, Thermo Fisher) into the water tank. The water tank was mounted on a translation stage (Newport, M-UMR12.40) to adjust the laser path length through water. Fluorescence was collected with a 20X water-immersion objective (Olympus XLUMPLFLN20x, NA = 1.0, WD = 2 mm) mounted on a Z-piezo stage (Jena, PZ 400 SG OEM). The signal passed through a short-pass filter (Semrock, FF01-750/SP-25) to block infrared light and a fluorescence emission filter (Semrock, FF01-630/69-25). The image was formed by a tube lens (Thorlabs, TTL180-A) and captured by an sCMOS camera (Hamamatsu C14440-20UP, 6.5 μm/pixel), yielding a field of view of 665×748 μm^2. We restricted imaging to a region of interest (ROI) around the laser, measuring 93×748 μm^2. The detection arm (comprising the imaging objective, tube lens, and camera) was also mounted on a translation stage to center the waist of the imaged beam within the field of view.

The light-sheet microscope system was controlled using a custom Matlab interface (R2020A, MathWorks) with a DAQ card (NI USB-6259, National Instruments) for data acquisition.

Beam propagation and waist dynamics were recorded under varying laser powers.

For the analysis of the steady-state experiments, we acquired an image stack of the laser beam consisting of 40 layers with 1 μm axial increments. We computed the axial projection of this stack and, for each line, extracted the position of maximum intensity. The beam radius was extracted as the distance from this maximum to the position where the intensity dropped to $1/e^2$ of the peak value.

For the analysis of the dynamic experiments, we recorded a single plane to achieve high temporal resolution. The waist position was extracted as the location of maximum fluorescence intensity.

3. Experimental results

3.1. Steady-state thermal lensing: focal shift and waist broadening

Figure 1(B) shows fluorescent images of the laser beam recorded at various laser powers after transient effects had subsided. As the laser power increases, the focal point shifts along the

Biomedical Optics EXPRESS

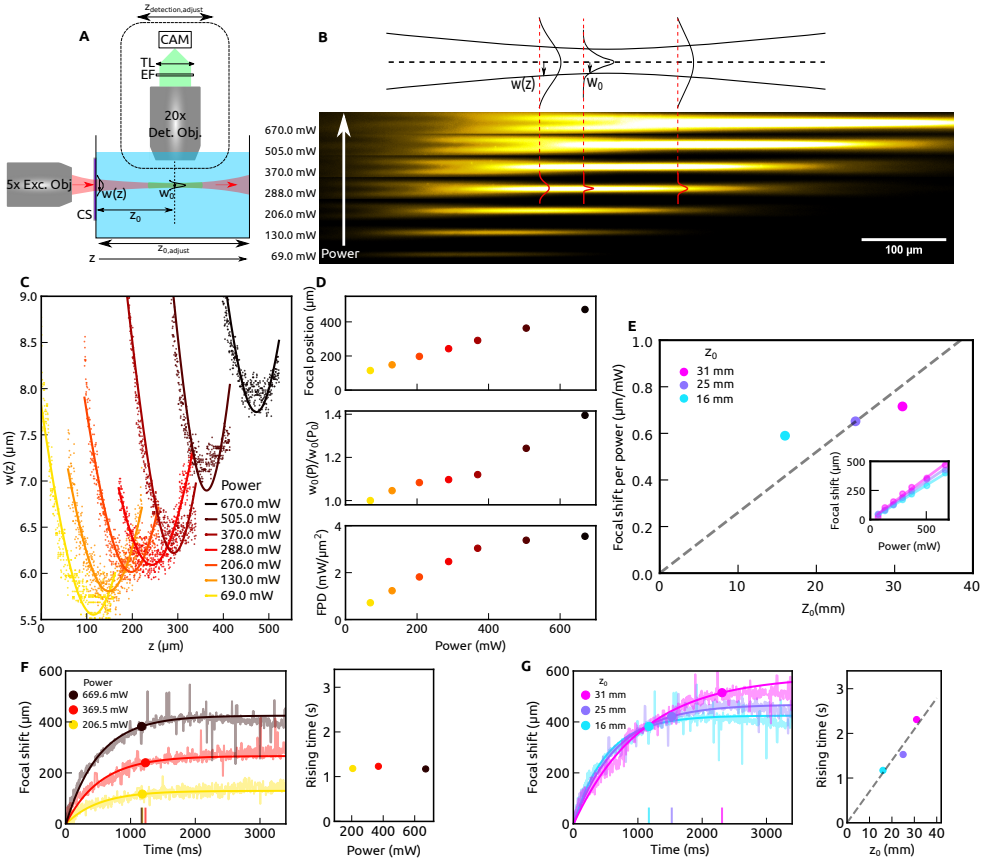

Fig. 1. (A) Profile and characteristic of the laser beam with increasing power, z_0 = 16 mm, RR = 50 MHz and λ = 1035 nm. (B) Images vertically stacked of beam propagating through water with increasing power. (C) Beam radius for several powers computed at $1/e^2$ from raw data and associated polynomial fit. (D) Focal shift, normalized waist, and focal power density as a function of power extracted from the fit of the axial beam profile shown in C. (E) Evolution of the slope of the focal shift with power for increasing z_0. Inset: Focal shift versus power for several z_0 (F) Left: Temporal evolution of the waist position for a laser beam in water, λ = 1035 nm, RR = 50 MHz, z_0 = 16 mm, framerate = 185 Hz, exponential fit (solid) based on maximum value reached from raw data (transparent) for three different power. Dots represent the 90% of max value of the exponential fit and associated so-called rising time. Right: Rising time for different power estimated on exponential fit from (left), error bars are calculated as standard error from the fit (G) Left: Temporal evolution of the waist position for a laser beam in water, λ = 1035 nm, RR = 50 MHz, Power = 669.6 mW, framerate = 185 Hz, exponential fit based on maximum value reached (solid) for three different z_0. Right: Rising time for different z_0 estimated on exponential fit from (left), error bars are calculated as standard error from the fit

direction of propagation while the beam waist expands. To quantify these changes, we determined the beam radius $w(z)$—the radial distance where the laser intensity dropped to $1/e^2$—as a function of the position along the propagation direction, z. The resulting axial profiles for different laser powers are shown in Fig. 1(C), with the focal position defined as the location of minimum beam width.

Biomedical Optics EXPRESS

Within the tested power range of 50–700 mW, the focal shift—defined as the difference in focus position relative to the lowest power configuration—increased linearly with laser power, reaching shifts of up to 0.4 mm at 700 mW (Fig. 1(D), top). A supralinear expansion of the beam waist accompanies this focal shift. We measured a relative enlargement of the beam waist of ~ 40% at maximum power (Fig. 1(D), center). In the absence of thermal lensing effects, the expected waist in water is 3.3 μm, calculated from the far-field beam divergence measured in air without the water tank. Our fluorescence-based measurement approach systematically overestimates the beam waist, which could be due to scattering effects (see Supplement 1 S - 1), particularly at small values of w_0. Thus, while the observed waist expansion is a genuine effect, its relative magnitude may in fact be underestimated due to this measurement bias. Additionally, we observed that the focal power density—defined as the ratio of laser power to illuminated surface area—tends to saturate at higher powers (Fig. 1(D), bottom).

Because thermal lensing can occur along the entire optical pathway, we further hypothesized that if local heating of the water is the underlying cause, the magnitude of the effect should depend on the optical path length through water. To test this, we repeated the experiments with three different path lengths: the original z_0 = 16 mm, z_0 = 25 mm, and z_0 = 31 mm. In all cases, the focal shift increased linearly with laser power (Fig. 1(F), inset), and the slope of this relationship became slightly steeper with increasing z_0 (Fig. 1(F)).

In summary, at steady state, the focal shift increased linearly with laser power, with a sensitivity that increased with the optical path length through water. In contrast, the waist broadening exhibited a supralinear dependence on power leading to a saturation of the focal power density.

3.2. Temporal dynamics of the focal shift

Figure 1(F) illustrates the temporal evolution of the beam waist position immediately after the laser is switched on. We used high-speed imaging to monitor the dynamic change in beam profile as the focal shift gradually approaches its steady state value. We found that the focal shift converges quasi-exponentially with a characteristic time constant on the order of a few seconds. Although the final focal shift increases with laser power, the transient dynamics remains largely independent of power, with a mean time constant of τ = 1.19 ± 0.015 s. Notably, increasing the laser propagation length through water (z_0) leads to a linear increase in the time constant required to reach steady state (Fig. 1(G)).

4. Numerical simulations

4.1. Thermal lens model

When a Gaussian laser beam propagates through a medium with a finite absorption coefficient, localized heating occurs due to energy deposition. This generates a paraxial temperature increase T, which alters the refractive index n via the thermo-optic effect. In water and most liquids, the thermo-optic coefficient $\mathrm{d}n/\mathrm{d}T$ is negative, meaning that the refractive index decreases with increasing temperature. Consequently, the refractive index is reduced along the beam axis and increases radially, forming an effective diverging lens—a phenomenon illustrated in Fig. 2.

Gordon et al. showed that the refractive index profile induced by the absorption of a Gaussian laser beam with beam waist w—defined as the radial distance at which the intensity drops to $1/e^2$ of its maximum—can be approximated near the optical axis by a parabolic function in a medium with initial refractive index n_0 [18].

$$n(r) = n_0 + \delta \cdot r^2 \tag{1}$$

Biomedical Optics EXPRESS

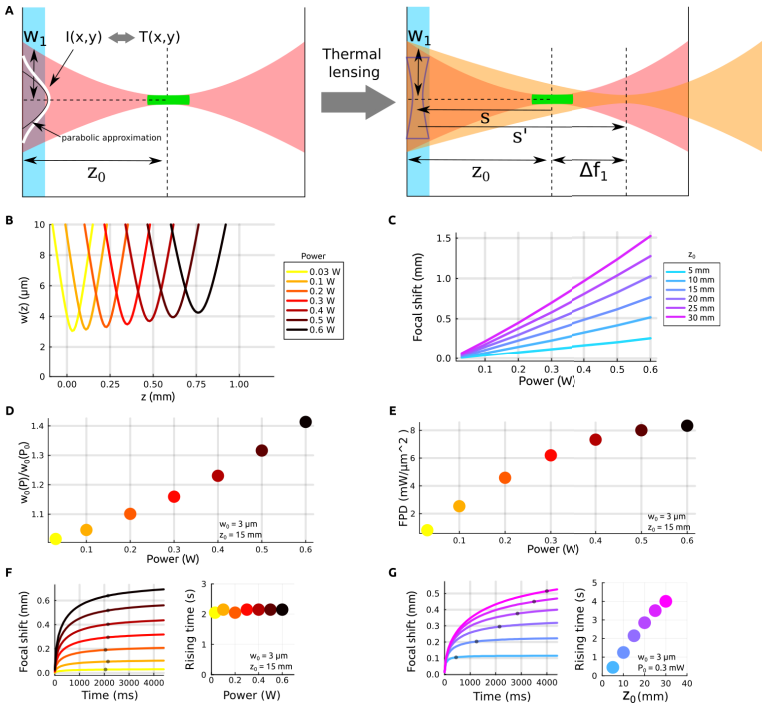

Fig. 2. Schematic of the model describing thermally induced focal shift. (A) A radial temperature gradient (white) is induced by the laser beam intensity profile (red). The path length through water is denoted z_0. We begin by modeling a thin water layer (blue), with the green area representing the initial focal region used in typical 2P-LSFM. This thin water layer acts as a weak diverging lens, producing a focal shift Δf_1. (B) Beam profiles for increasing laser power. (C) Focal shift as a function of power for increasing z_0. (D) Beam waist normalized to its value at the lowest power, plotted as a function of laser power. (E) Focal power density (FPD) as a function of laser power. (F) Temporal evolution of the focal shift for different z_0. (G) Temporal evolution of the focal shift for different laser powers. The grey dots in F and G represent the time to reach 90% of the maximum value calculated at t = 3s

Within the thin-lens approximation, the corresponding focal length of the thermal lens at steady state is given by:

$$F_{ss}(w) = -\frac{2}{1.3}\frac{n_0}{l}\frac{1}{2\delta} = \frac{n_0}{l}\frac{\pi k w^2}{P\alpha l\frac{dn}{dT}} \tag{2}$$

Here, l is the thickness of the absorbing element, k its thermal conductivity, w the beam radius at the position of the element, P the laser power, α the absorption coefficient, and $\frac{dn}{dT}$ the thermo-optic coefficient. The factor $\frac{2}{1.3}$ arises when the parabolic approximation is constrained to pass through the value of the exact solution at the beam radius w (see Supplement 1 S - 2).

To determine the focal shift introduced by a thin thermal lens located at a distance s_i from the laser waist (with s_i<0 indicating a position before the waist), we apply the standard Gaussian optics lens formula [15]:

$$\Delta f_i = s_i + s_i' = s_i + \frac{\frac{z_r^2}{F} - s_i\left(1 - \frac{s_i}{F}\right)}{\frac{z_r^2}{F^2} + \left(1 - \frac{s_i}{F}\right)^2} \tag{3}$$

Biomedical Optics EXPRESS

where $z_r = \pi w_0^2/\lambda$ is the Rayleigh range, and $s_i\prime$ is the distance from the lens to the new image plane of the beam waist.

Crucially, because the beam is focused inside the water volume, the beam radius varies along the propagation axis. Consequently, each water layer introduces a local, thin diverging lens whose effect depends on the beam size at that location, which itself is modified by preceding thermal lenses. As a result, the overall focal shift arises from these thermal lenses' cumulative, interdependent effects. We numerically computed the total focal shift, $\Delta f_{tot} = \sum_i \Delta f_i$, from this cumulative effect using an iterative scheme with 10 μm-thick water layers for steady state simulations and 1 μm-thick layers for simulations of temporal dynamics.

Gordon et al. also derived the characteristic time τ over which the thermal lens forms under continuous laser heating, showing that it is governed by heat diffusion over the characteristic length scale set by the beam radius:

$$\tau = \frac{w^2}{4D} \tag{4}$$

where $D = \frac{\kappa}{\rho c_p}$ is the thermal diffusivity of the medium, with κ denoting thermal conductivity, ρ the density, and c_p the specific heat capacity.

Accordingly, the focal length of the thermal lens under continuous laser illumination at constant power evolves over time, approaching its steady-state value as:

$$F(t, w) = F_{ss}(w)\left[1 + \frac{\tau}{2t}\right] \tag{5}$$

Using this formula in our iterative simulation code, we also simulated the temporal evolution of both the focal shift and the waist broadening.

For all simulations, we used a beam waist $w_0 = 3.0\ \mu$m, consistent with the theoretical value expected from our experimental setup described above. All other parameters used in the model are listed in Table 1.

Table 1. Simulation Parameters

λ	1035 nm	wavelength
κ	0.6 W.kg $^{-1}$.K^{-1}	thermal conductivity
α	19 m^{-1}	absorption coefficient at 1035 nm (from [19])
$\frac{dn}{dT}$	-1.1 × 10^{-4} K^{-1}	thermo-optic coefficient at 20 °C [20]
c_p	4186J.kg^{-1}.K^{-1}	heat capacity
ρ	1000 kg.m^{-3}	density

4.2. Simulation results

4.2.1. Steady-state thermal lensing: focal shift and waist broadening

Our simulations (see Fig. 2 and Table 1) successfully reproduce the scaling of both the axial shift and distortion of the laser intensity profile that give rise to focal shift and waist broadening as laser power increases.

Consistent with experimental observations, the simulated focal shift exhibits a linear dependence on laser power, with a sensitivity that increases linearly with z_0, the distance traveled by the laser before reaching its focal point. This result is, at first glance, counterintuitive. According to Eq. (2), the focal length of the induced thermal lens is proportional to the Gaussian beam's radius. The Gaussian beam has a large radius at large distances from the geometric focal point, resulting in a weakly divergent thermal lens with a long focal length. One might therefore expect the contribution of these distant water layers to the overall focal shift to be negligible. However, due to the beam geometry and in the limit where $1/F \ll 1$, the focal shift induced by each differential

Biomedical Optics EXPRESS

layer becomes approximately constant, with deviations occurring only for water layers within the Rayleigh range of the laser beam. As a result, the total focal shift increases linearly with z_0 and is given by Eq. (6) (see the Supplement 1 S - 2 for the calculation and comparison to the simulations).

$$\Delta f_{\text{tot}} \approx -\frac{1.3}{2} \frac{\pi\, n_w\, \alpha\, \frac{dn}{dT}}{\kappa\, \lambda^2} \cdot w_0^2 \cdot P \cdot z_0 \tag{6}$$

This equation also reveals a quadratic dependence of the focal shift on the beam waist and on the inverse of the wavelength. In addition, both the optical absorption and the thermo-optic coefficient are wavelength-dependent, further influencing the total shift.

The simulation also reproduces the supralinear increase in waist broadening with laser power, which we observed experimentally. The model predicts that, as a direct consequence of this dependency, the focal power density may reach a maximum because laser power increases linearly while the waist broadens supralinearly (see Fig. 2(E)). Beyond this maximum point, further increases in laser power should result in a reduction in fluorescence excitation due to the two-photon effect, despite the higher total power.

4.2.2. Temporal dynamics of the focal shift

Our simulations also reproduce the quasi-exponential approach to steady state, with a time constant that is independent of laser power and scales linearly with z_0, reflecting the cumulative thermal effect along the optical path.

Since $\tau \propto w^2$, the thermal lens near the waist—where the beam radius is smallest—reaches steady state within a few milliseconds. In contrast, water layers located several millimeters or centimeters away from the focus, where the beam radius is much larger, require significantly longer timescales (up to seconds) to equilibrate. This implies that the most distant water layers define the time required to reach thermal equilibrium. The parameter z_0—the distance traveled through water before reaching the focus—is thus a key determinant of the system's temporal response.

5. Conclusion and discussion

This study demonstrates that thermal lensing markedly alters the beam waist in 2P-LSFM, both in its position and size. As laser power increases, we experimentally observe a linear focal shift of up to 0.3 mm at 500 mW—power levels typical for fast volumetric calcium imaging in larval zebrafish—and a nonlinear beam waist broadening, reaching approximately 20% of its original diameter. These distortions degrade optical sectioning, and can introduce fluorescence fluctuations over time, potentially confounding the interpretation of functional recordings.

Our results further indicate that the extent of thermal lensing is influenced by the laser's propagation distance through water. Longer water paths exacerbate the lensing effects, which is particularly critical for imaging large samples or when a large field of view is required. This dependency emphasizes the need for careful optical design in systems where extended water paths are unavoidable.

To better understand these effects, we developed a theoretical model that captures the spatial and temporal scaling of thermal lensing as functions of laser power, propagation distance, and time. Although the model qualitatively reproduces our experimental observations, it systematically overestimates the magnitude of the focal shift by a factor of approximately two, as well as the dependence on z_0. This discrepancy likely arises because the model accounts only for heat conduction, neglecting convective effects. Indeed, we observe signatures of convection in the temporal evolution of the focal shift that initially increases, reaches a maximum, and then gradually decreases after approximately two seconds, suggesting a dynamic redistribution of the heated fluid. This redistribution leads to lower steady-state focal shifts than those predicted by the model. This observation was also reported in the original study by Gordon *et al.* [18].

Biomedical Optics EXPRESS

In the pure conduction model (paraxial, weak-lens limit), the thermally induced focal shift scales linearly with both laser power and propagation distance ($\Delta z_{\text{tot}} \propto P z_0$). Experimentally, we observe a robust linear increase in focal shift with power for each propagation distance tested. However, the slope of this relationship changes only weakly when z_0 is increased from 16 mm to 31 mm (roughly 0.6 to 0.7 μm/mW), far less than the proportional change predicted by the model. We attribute this reduced z_0-sensitivity to buoyancy-driven convection shaped by the microscope's geometry: the excitation beam propagates horizontally beneath the detection objective, which sits approximately 2 mm above the focus with a 5 mm clear aperture and then widens conically at ~45°. Heated fluid rising from the beam is partially confined beneath the objective nose and must spread laterally before escaping upward at the edge. Farther along the beam path, where the vertical clearance increases, warm fluid is more efficiently removed by convection, reducing the local temperature rise and thus the refractive-index change. As a result, only a finite axial region near the beam waist remains thermally active, and increasing the geometric water path beyond this region contributes progressively less to the cumulative thermal lens.

Increasing the mean excitation power is a common strategy in multiphoton imaging to enhance signal intensity, reduce illumination time, and accelerate volumetric acquisition. However, this approach is fundamentally limited by well-known biological constraints, including phototoxicity, photobleaching, and heat-induced damage to the sample. Our results add an important optical consideration: even at laser powers typically used for physiological imaging, thermal lensing introduces significant beam degradation, which can compromise both image quality and spatial resolution. In our analysis, we modeled the thermal lens as a thin lens with a parabolic refractive index profile. However, deviations from this idealized shape give rise to spherical aberrations that distort the laser focus and contribute to further broadening of the beam waist. These cumulative effects may be especially problematic in advanced illumination techniques that rely on complex beam shaping, such as Bessel-beam light sheets, where thermally induced aberrations could impact the optical sectioning performance.

These limitations are directly relevant to the practical workflow of 2P-LSFM. A notable challenge arises during the transition from low-power alignment (~50 mW) to high-power imaging conditions (400–500 mW). At low power, precise centering of the laser waist within the field of view is readily achieved. However, under high-power conditions, thermal lensing induces both lateral displacement and broadening of the waist, leading to resolution loss, particularly in the central imaging region. While these power levels may appear high, it is worth noting that some *in vivo* studies have demonstrated the safe use of average powers from 200 to 500 mW under appropriate optical configurations (e.g., longer wavelengths and moderate repetition rates) [14,21]. This reinforces the relevance of our findings for biological applications and underscores the importance of accounting for power-dependent optical distortions during system alignment and calibration.

Beyond steady-state effects, our study highlights the dynamic nature of thermal lensing. The beam waist evolves over time, following a quasi-exponential saturation with a characteristic time constant on the order of seconds. These transient dynamics have the potential to interfere with imaging in time-varying sample environments. For example, during stepwise repositioning in large-volumetric scans, thermal lensing could introduce spatial inhomogeneities in the illumination pattern across the sample. This concern becomes even more relevant when considering the extension of 2P-LSFM to specific configurations of functional imaging of neural activity. Several advanced experimental paradigms—such as flow-based delivery of chemical [22] or hydrodynamic stimuli [23], whole-microscope rotation for vestibular stimulation [7,24], and setups that allow for functional imaging in freely swimming fish [25]—have been successfully implemented using one-photon light-sheet microscopy, where thermal lensing is negligible due to the lower absorption of visible light. However, adapting these strategies to two-photon configurations

Biomedical Optics EXPRESS

would increase sensitivity to heat-induced refractive index changes in the medium. In such contexts, dynamic focal shifts caused by thermal lensing could significantly compromise signal fidelity, particularly when the timescale of stimulus delivery or sample movement approaches the thermal settling time. Under these conditions, fluorescence changes arising from beam waist drift may coincide with stimulus-evoked or behaviorally driven neural activity, confounding the interpretation of calcium signals and introducing artifacts into functional recordings. These considerations emphasize the importance of accounting for thermal dynamics when designing experimental protocols for use with high-power 2P-LSFM systems.

The implications of our findings extend beyond passive mitigation of image degradation. A deeper understanding of the interplay between laser power, propagation distance, and thermal dynamics could pave the way for actively controlling beam propagation in high-power 2P-LSFM systems. For instance, adaptive optics or real-time feedback mechanisms could be used not only to restore image quality by correcting for focal shifts and beam broadening, but also to enable more stable and precise illumination conditions.

Beyond the specific context of light-sheet microscopy, our findings suggest that thermal lensing may also be considered in multiphoton imaging systems, particularly at high powers or when using wavelengths with significant water absorption, such as 1300 nm or 1700 nm, commonly used in three-photon (3P) microscopy. Although multiphoton objectives typically have high numerical apertures and short working distances, limiting the optical path through water to just a few millimeters, thermal effects can still arise under these conditions. We estimate focal shifts up to 10 μm at 1700 nm and 300 mW (see Supplement 1 S - 3). While these effects may be subtle, they could become critical in experiments that demand precise spatial targeting, such as optogenetic stimulation or subcellular imaging. In such cases, thermal lensing could lead to misalignment between the intended and actual focal planes, compromising the accuracy of both stimulation and signal detection.

In summary, this work is, to our knowledge, the first report of thermal lensing in light-sheet fluorescence microscopy. The phenomenon, emerging under high-power IR excitation and extended water paths, may have been overlooked in traditional high-resolution setups that employ short working distances and high-NA objectives. Ultimately, a thorough understanding and effective control of thermal lensing are essential for optimizing 2P-LSFM performance, particularly in demanding applications such as functional imaging in live specimens. Future work should focus on integrating compensation techniques to mitigate these thermal effects, ensuring reliable and high-quality imaging outcomes.

Funding. European Research Council (ERC, grant no. 715980); Région Île-de-France, Domaine d'intérêt Majeur (DIM) ELICIT program, (project FAST2P); Région Île-de-France, ARDoC doctoral funding program (grant no. 17012950); Centre National de la Recherche Scientifique (CNRS); Sorbonne Université (i-Bio Postdoctoral Fellowship)

Acknowledgements. We are grateful to Carounagarane Dore for his contribution to the design of the experimental setup. This project has received funding from the European Research Council (ERC) under the European Union's Horizon 2020 research innovation program, grant agreement number 715980. Furthermore, it was supported by grants from Région Ile-de-France, through the Domaine d'Intérêt Majeur (DIM) ELICIT program (project FAST2P). Moreover, the project received partial funding from the CNRS and Sorbonne Université. AH was partially funded by a PostDoc fellowship from the i-Bio initiative at Sorbonne University, and HT had a Ph.D. fellowship from Ile de France (ARDoC 17012950).

Contributions. AH, HT, TP, GD, and VB designed the project, conducted research, analyzed data, performed simulations, and wrote the manuscript.

Disclosures. The authors declare no conflict of interest.

Data availability. Analysis scripts, data underlying the figures and simulation code are available at [26].

Supplemental document. See Supplement 1 for supporting content.

References

1. J. Huisken, J. Swoger, F. Del Bene, *et al.*, "Optical sectioning deep inside live embryos by selective plane illumination microscopy," Science **305**(5686), 1007–1009 (2004).

Biomedical Optics EXPRESS

2. P. J. Keller, A. D. Schmidt, J. Wittbrodt, *et al.*, "Reconstruction of zebrafish early embryonic development by scanned light sheet microscopy," Science **322**(5904), 1065–1069 (2008).
3. F. F. Voigt, D. Kirschenbaum, E. Platonova, *et al.*, "The mesospim initiative: open-source light-sheet microscopes for imaging cleared tissue," Nat. Methods **16**(11), 1105–1108 (2019).
4. B. Yang, M. Lange, A. Millett-Sikking, *et al.*, "Daxi–high-resolution, large imaging volume and multi-view single-objective light-sheet microscopy," Nat. Methods **19**(4), 461–469 (2022).
5. T. Panier, S. A. Romano, R. Olive, *et al.*, "Fast functional imaging of multiple brain regions in intact zebrafish larvae using selective plane illumination microscopy," Front. Neural Circuits **7**, 65 (2013).
6. M. B. Ahrens, M. B. Orger, D. N. Robson, *et al.*, "Whole-brain functional imaging at cellular resolution using light-sheet microscopy," Nat. Methods **10**(5), 413–420 (2013).
7. G. Migault, T. L. van der Plas, H. Trentesaux, *et al.*, "Whole-brain calcium imaging during physiological vestibular stimulation in larval zebrafish," Curr. Biol. **28**(23), 3723–3735.e6 (2018).
8. T. V. Truong, W. Supatto, D. S. Koos, *et al.*, "Deep and fast live imaging with two-photon scanned light-sheet microscopy," Nat. Methods **8**(9), 757–760 (2011).
9. F. O. Fahrbach, V. Gurchenkov, K. Alessandri, *et al.*, "Light-sheet microscopy in thick media using scanned Bessel beams and two-photon fluorescence excitation," Opt. Express **21**(11), 13824 (2013).
10. P. Mahou, J. Vermot, E. Beaurepaire, *et al.*, "Multicolor two-photon light-sheet microscopy," Nat. Methods **11**(6), 600–601 (2014).
11. A. Escobet-Montalbán, F. M. Gasparoli, J. Nylk, *et al.*, "Three-photon light-sheet fluorescence microscopy," Opt. Lett. **43**(21), 5484–5487 (2018).
12. S. Wolf, W. Supatto, G. Debrégeas, *et al.*, "Whole-brain functional imaging with two-photon light-sheet microscopy," Nat. Methods **12**(5), 379–380 (2015).
13. S. Hartmann, R. Vogt, J. Kunze, *et al.*, "Zebrafish larvae show negative phototaxis to near-infrared light," PLoS One **13**(11), e0207264 (2018).
14. V. Maioli, A. Boniface, P. Mahou, *et al.*, "Fast in vivo multiphoton light-sheet microscopy with optimal pulse frequency," Biomed. Opt. Express **11**(10), 6012–6026 (2020).
15. C. Simonelli, E. Neri, A. Ciamei, *et al.*, "Realization of a high power optical trapping setup free from thermal lensing effects," Opt. Express **27**(19), 27215–27228 (2019).
16. P. Loiko, F. Druon, P. Georges, *et al.*, "Thermo-optic characterization of yb: Cagdalo4 laser crystal," Opt. Mater. Express **4**(11), 2241–2249 (2014).
17. V. Pilla, E. Munin, and M. R. Gesualdi, "Measurement of the thermo-optic coefficient in liquids by laser-induced conical diffractionand thermal lens techniques," J. Opt. A: Pure Appl. Opt. **11**(10), 105201 (2009).
18. J. Gordon, R. Leite, R. Moore, *et al.*, "Long-transient effects in lasers with inserted liquid samples," J. Appl. Phys. **36**(1), 3–8 (1965).
19. G. M. Hale and M. R. Querry, "Optical constants of water in the 200-nm to 200-μm wavelength region," Appl. Opt. **12**(3), 555–563 (1973).
20. G. Abbate, U. Bernini, E. Ragozzino, *et al.*, "The temperature dependence of the refractive index of water," J. Phys. D: Appl. Phys. **11**(8), 1167–1172 (1978).
21. S. Takanezawa, T. Saitou, and T. Imamura, "Wide field light-sheet microscopy with lens-axicon controlled two-photon bessel beam illumination," Nat. Commun. **12**(1), 2979 (2021).
22. R. Candelier, M. S. Murmu, S. A. Romano, *et al.*, "A microfluidic device to study neuronal and motor responses to acute chemical stimuli in zebrafish," Sci. Rep. **5**(1), 12196 (2015).
23. G. Vanwalleghem, K. Schuster, M. A. Taylor, *et al.*, "Brain-wide mapping of water flow perception in zebrafish," The Journal of Neuroscience **40**(21), 4130–4144 (2020).
24. G. Migault, N. Beiza-Canelo, S. Chatterjee, *et al.*, "Distinct and asymmetric neuronal responses to pitch-and roll-axis vestibular stimulation in larval zebrafish," bioRxiv (2024).
25. D. H. Kim, J. Kim, J. C. Marques, *et al.*, "Pan-neuronal calcium imaging with cellular resolution in freely swimming zebrafish," Nat. Methods **14**(11), 1107–1114 (2017).
26. A. Hubert, H. Trentesaux, T. Pujol, *et al.*, "Thermal lensing effects in two-photon light-sheet microscopy: data and simulation code," Github, 2025, https://github.com/LJPZebra/ThermalLens.git